Journal of
Materials Chemistry A

Materials for energy and sustainability

rsc.li/materials-a

PAPER
Zhitian Liu, Biao Gao, Paul K. Chu *et al.*
Energy-saving hydrogen production by the methanol oxidation reaction coupled with the hydrogen evolution reaction co-catalyzed by a phase separation induced heterostructure

ROYAL SOCIETY OF CHEMISTRY

ROYAL SOCIETY OF CHEMISTRY

PAPER

Check for updates

Energy-saving hydrogen production by the methanol oxidation reaction coupled with the hydrogen evolution reaction co-catalyzed by a phase separation induced heterostructure †

Xiang Peng, [ab] Song Xie,[a] Xia Wang, [a] Chaoran Pi,[c] Zhitian Liu,*[a] Biao Gao, *[bc] Liangsheng Hu, [d] Wei Xiao [e] and Paul K. Chu *[b]

Electrochemical water splitting is a desirable technique to produce hydrogen to replace fossil fuels for sustainable energy generation. However, efficient hydrogen production suffers from a sluggish oxygen evolution reaction (OER) and expensive electrocatalysts. Herein, the methanol oxidation reaction (MOR) is combined with the hydrogen evolution reaction (HER) to achieve energy-saving hydrogen production. The HER and MOR are co-catalyzed by a bifunctional electrocatalyst containing a $NiSe/MoSe_2$ heterointerface on carbon cloth (NMS/CC). The electronic structure rearrangement and charge transfer at the heterointerface are investigated experimentally and theoretically. The NMS/CC electrocatalyst has outstanding MOR properties requiring a smaller potential and Tafel slope than those of the OER as well as high efficiency and stability. Energy-saving hydrogen production by the combined MOR/HER configuration can be powered by a solar cell with an output voltage of 1.5 V. The results reveal the excellent prospect of this novel strategy for zero-carbon-emission energy generation and provide insights into the coordination of electrosynthesis and electrocatalysis.

1 Introduction

Hydrogen is one of the desirable substitutes for fossil fuels in the pursuit of green energy on account of its large energy density and zero-carbon footprint.[1–3] Electrochemical water electrolysis composed of hydrogen evolution reaction (HER) on the cathode and oxygen evolution reaction (OER) on the anode is one of the promising techniques to produce high-purity hydrogen gas.[4–7] In overall water splitting, OER is the rate-determining step with a theoretical voltage as high as 1.23 V in addition to high overpotentials in both HER and OER in conjunction with high energy consumption.[8–10] Decreasing the overpotential in either HER or OER is important to energy saving.[11–13] In addition, the mixed product of hydrogen and oxygen is not only hazardous but also difficult to separate. Therefore, to improve the energy economy and safety of hydrogen production, HER should be coupled with an effective anodic oxidation reaction without producing gas products. In this respect, economical and earth-abundant high-performance electrocatalysts are crucial to the two semi-reactions.

Efforts have been made to decrease the energy barrier of the anodic oxidation reaction for energy-saving hydrogen production by designing economical and earth-abundant high-performance electrocatalysts for both semi-reactions. For instance, Xu *et al.* have shown superior catalytic activity of the urea oxidation reaction (UOR) including a voltage of 1.33 V to generate a current density of 50 mA cm^{-2}, which is smaller than those of NiMo-based catalysts.[14] Zhang *et al.* have replaced the OER with the UOR for energy-saving hydrogen production and the potential required for UOR decreases by 340 mV compared to the conventional OER.[15] The UOR is associated with a six-electron conversion process, which is more complex than OER. Moreover, the product of the combined UOR/HER overall reaction is a gas mixture such as $H_2/N_2/CO_2$ and so further purification and carbon emission are inevitable. Methanol can

[a]Hubei Key Laboratory of Plasma Chemistry and Advanced Materials, Hubei Engineering Technology Research Center of Optoelectronic and New Energy Materials, Wuhan Institute of Technology, Wuhan, 430205, China. E-mail: able. ztliu@wit.edu.cn

[b]Department of Physics, Department of Materials Science and Engineering, Department of Biomedical Engineering, City University of Hong Kong, Tat Chee Avenue, Kowloon, Hong Kong, China. E-mail: paul.chu@cityu.edu.hk

[c]State Key Laboratory of Refractories and Metallurgy and Institute of Advanced Materials and Nanotechnology, Wuhan University of Science and Technology, Wuhan, 430081, China. E-mail: gaobiao@wust.edu.cn

[d]Department of Chemistry and Key Laboratory for Preparation and Application of Ordered Structural Materials of Guangdong Province, Shantou University, Shantou, 515063, Guangdong, China

[e]School of Resource and Environmental Sciences, Hubei International Scientific and Technological Cooperation Base of Sustainable Resource and Energy, Wuhan University, Wuhan, 430072, China

† Electronic supplementary information (ESI) available. See https://doi.org/10.1039/d2ta02955c

This journal is © The Royal Society of Chemistry 2022

J. Mater. Chem. A, 2022, **10**, 20761–20769 | **20761**

be converted into soluble and value-added formate by the electrochemical methanol oxidation reaction (MOR) that requires lower overpotentials than OER.[16] Recently, Zhao *et al.* have proposed active and stable electrocatalysis by converting methanol into formate at a high and steady current density ($\sim$345 mA cm^{-2}) with high faradaic efficiency (>95%).[17] Therefore, it is possible to generate high-purity hydrogen directly by the MOR coupled with the HER. Unfortunately, the optimal match between the HER and MOR and associated MOR/HER mechanisms are still not well understood.

To realize the energy-saving hydrogen production implements of MOR/HER coupling system, a bifunctional electrocatalyst with high efficiency and long-term stability for both HER and MOR is essential. Non-noble transition metal-based electrocatalysts have been investigated for electrochemical water splitting due to the low-cost and large abundance.[18–21] Experimental studies have shown that Ni(Co)-based materials show considerable methanol oxidation characteristics.[22] Moreover, the Mo-based compounds are attractive and inexpensive substitutes for Pt-group electrocatalysts in the basic environment because of their low binding energy with hydrogen.[23] Thus, constructing a heterojunction comprising Mo and Ni(Co) components is predicted to take a prominent effect on MOR/HER hydrogen generation. Previously, our research group proposed and demonstrated a bifunctional Ni(Co)/Mo selenide heterostructured electrocatalyst is an ideal platform for OER/HER in overall water splitting.[24] However, the atomic interactions at the heterointerface, the catalytic mechanism of the MOR/HER, and the optimization of Ni(Mo)-based heterostructural electrocatalyst for HER and MOR have not been investigated systematically.

Herein, the combined MOR/HER technique illustrated schematically in Scheme 1 is demonstrated for energy-saving hydrogen production and the integrated system can be driven by solar cells with the output voltage of 1.5 V. The HER and MOR are co-catalyzed by a bifunctional electrocatalyst composed of heterostructured NiSe and MoSe$_2$ synthesized on carbon cloth (NMS/CC). The electronic structure rearrangement, as well as interactions between interfacial atoms, is investigated experimentally and theoretically. The hierarchical structure boasts high MOR efficiency such as a potential that is 15% less than that in the OER at a current density of 100 mA cm^{-2} as well as a small Tafel slope of 14 mV dec^{-1}, which is only 7% of that in the OER. The heterointerface between MoSe$_2$ and NiSe balances the adsorption energy of the reactants/intermediates/products and promotes the MOR/HER kinetics. As a result, the MOR/HER couple shows a voltage decrease of 8% compared to the OER/HER system in hydrogen production and no product purification is required.

2 Experimental

2.1 Materials preparation

The nickel molybdate nanowire arrays were prepared on carbon cloth (CC) hydrothermally. In the process, 1.5 mmol NiCl$_2$·6H$_2$O and 1.5 mmol Na$_2$MoO$_4$·2H$_2$O were dissolved in 30 mL of deionized water (DW) under vigorous stirring for 30 min before transferring to a 50 mL Teflon container. A piece of clean CC (2×3 cm^2) was immersed in the solution in the container, which was heated to 130 °C for 12 h in an autoclave. The NiMoO$_4$-covered CC (denoted as NMO/CC) was produced by annealing the hydrothermal product at 400 °C in N$_2$ for 1 h at a ramp rate of 5 °C min^{-1}.

The heterostructure was prepared by a selenation process. NMO/CC and Se powder were put on two separate porcelain plates with Se powder upstream in a tube furnace. The sample
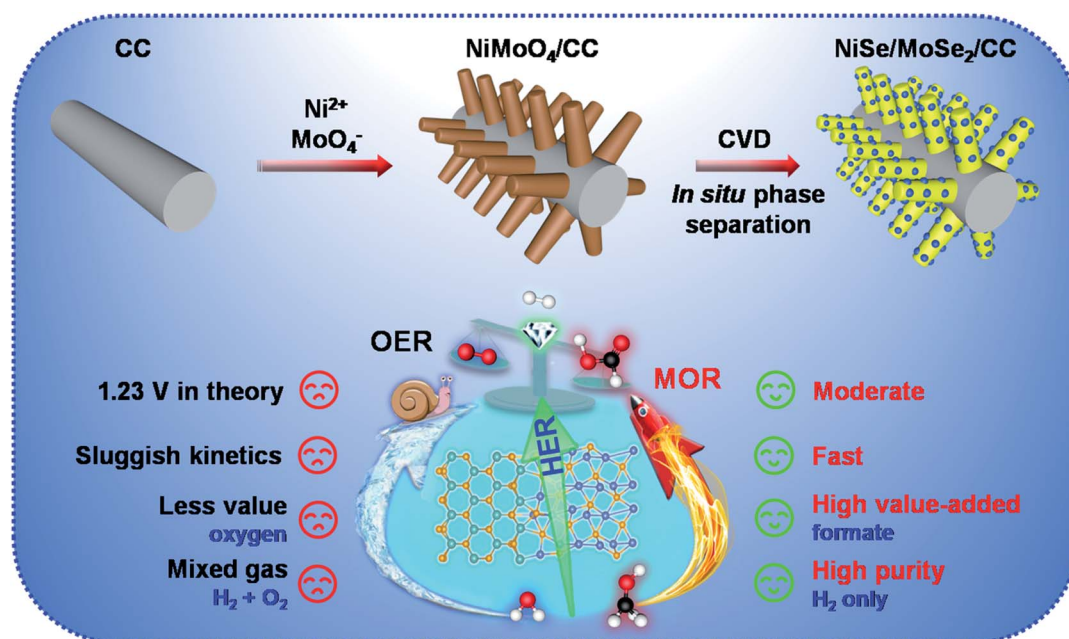
Scheme 1 Schematic illustration of the preparation of the bifunctional NMS/CC electrocatalyst and application for MOR-coupled energy-saving hydrogen production.

was heated to 400 °C for 1 h at a rate of 5 °C min^{-1} under flowing N_2/H_2 (containing 8% H_2) and then cooled to room temperature naturally afterwards. The NMS/CC was obtained. For comparison, pure Ni/Mo-based selenide was prepared on CC as described in the ESI† and the samples were labelled NiSe/CC and MoSe$_2$/CC, respectively.

2.2 Materials characterization

The morphology of the samples was examined by scanning electron microscopy (SEM, FEI/Philips XL30 Esem-FEG) and transmission electron microscopy (TEM, FEI/Philips Tecnai 12 BioTWIN) coupled with energy-dispersive X-ray (EDX) spectroscopy. The composition and crystal structure were determined by high-resolution TEM (HR-TEM), X-ray diffraction (XRD, LabX XRD-6100, Shimadzu) with a Cu K_α source, Raman scattering (HR RamLab), and X-ray photoelectron spectroscopy (XPS, Thermo Scientific K-Alpha, Thermo Fisher) using monochromatic Al K_α X-rays. The X-ray absorption spectra at the Mo

and Ni K-edges are collected at the 1W1B station of the Beijing Synchrotron Radiation Facility (BSRF), China. Ni foil and Mo foil were used to calibrate the energy. The ^{1}H-NMR spectra were acquired on a Bruker Avance III-HD-400 MHz spectrometer in dimethyl sulfoxide at 298 K. The electrical conductivity of the electrocatalysts was determined by using a four-point probe on a Keithley 2450.

2.3 Electrochemical measurement

The electrochemical measurements were performed on a CHI 760E electrochemical workstation (Shanghai CH Instrument, China) in an aqueous solution containing 1.0 M KOH and 1.0 M methanol. Linear sweep voltammetry (LSV) was conducted using a three-electrode configuration in which a graphite rod was the counter electrode, a saturated calomel electrode (SCE) was the reference electrode, and modified CC served as the working electrode at a scan rate of 5 mV s^{-1}. All the potentials were iR corrected and referenced to the reversible hydrogen
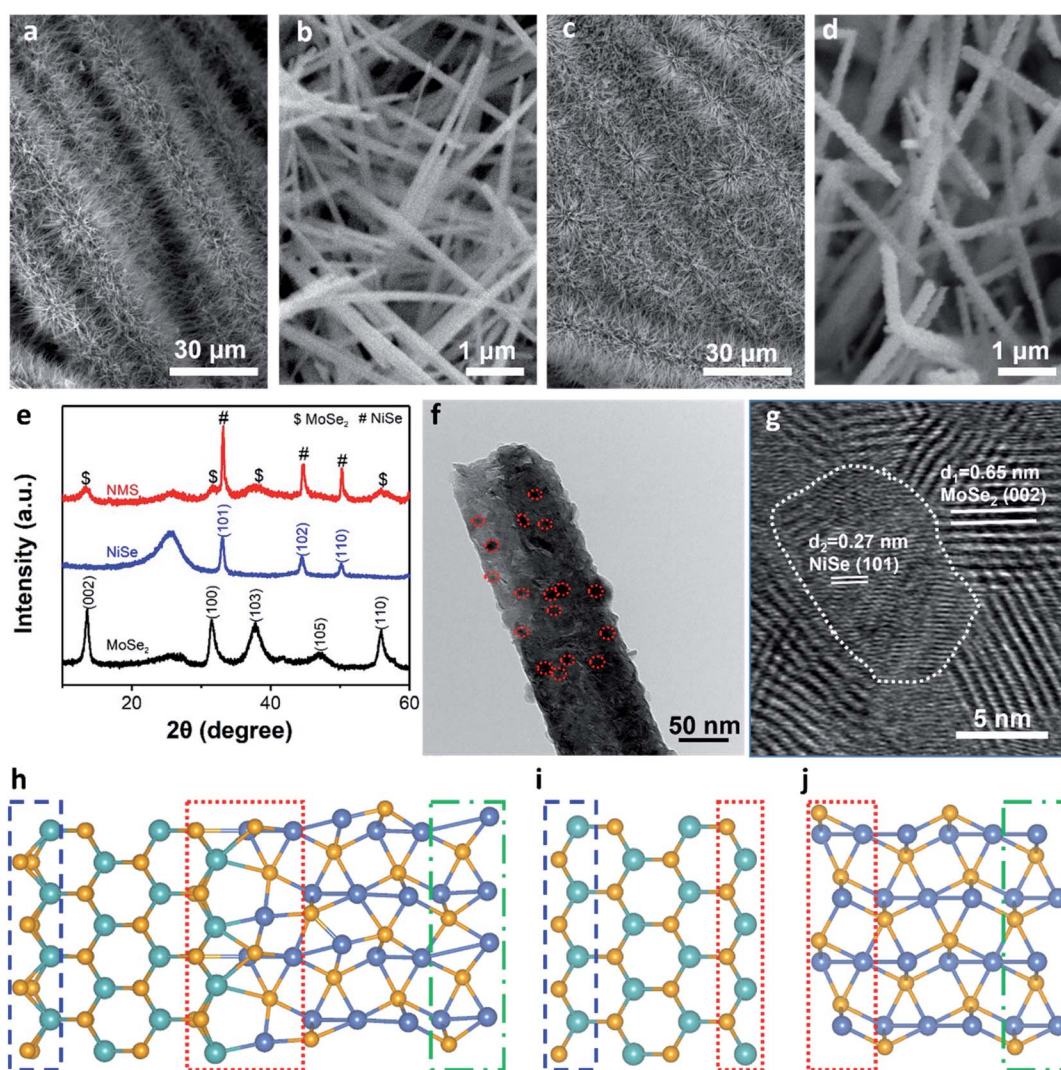

Fig. 1 SEM images of (a and b) NMO/CC and (c and d) NMS/CC; (e) XRD spectra of NMS/CC, NiSe/CC, and MoSe$_2$/CC; (f) TEM image (red circles indicate particles anchored on the nanowire) and (g) HR-TEM image of the NMS nanowire. Top view of (h) the simulated NiSe (101)/MoSe$_2$ (002) heterointerface, and (i) individual MoSe$_2$ (002) and (j) NiSe (101) surfaces (brown color represents Se, cyan represents Mo, and bice represents Ni).

This journal is © The Royal Society of Chemistry 2022

J. Mater. Chem. A, 2022, **10**, 20761–20769 | **20763**

electrode (RHE) according to the Nernst equation E (RHE) = E (SCE) + 0.242 + 0.059 × pH. The pH of the 1.0 M KOH solution was measured to be 13.51 (FE28, Mettler Toledo). The Tafel slope was calculated by fitting the linear portion of the Tafel plot. Electrochemical impedance spectroscopy (EIS) was carried out with an amplitude of 5 mV in the frequency range of 100 kHz–0.1 Hz. The electrochemically active surface area (ECSA) was determined by cyclic voltammetry (CV) in the voltage range between −0.5 V and −0.6 V $vs.$ SCE. The stability was evaluated at potentials (voltage) of −0.21 V $vs.$ RHE for the HER, 1.41 V $vs.$ RHE for the MOR, and 1.80 V for the overall reaction.

3   Results and discussion

3.1   Materials structure

The SEM images in Fig. 1a and b show that uniform nanowire arrays with a smooth surface cover the carbon fibers. After selenation, Fig. 1c and d show that the array structure remains, but the nanowires become rough and there are nanoparticles on the surface providing more active sites for electrocatalysis. The crystal structure of the samples is determined by XRD. The diffraction pattern of the hydrothermal product (NMO/CC) can be indexed to NiMoO$_4$ containing α-NiMoO$_4$ (JCPDS 33-0948) and β-NiMoO$_4$ (JCPDS 45-0142) as shown in Fig. S1,† except the small peak shift associated with combined water (Fig. S2†).[25,26] After selenation at 400 °C, NiMoO$_4$ is converted into the composite of NiSe (JCPDS 02-0892) and MoSe$_2$ (JCPDS 77-1715) as shown in Fig. 1e, including a diffraction peak at ∼26° from the CC skeleton. The mono-metal-based products are pure NiSe and MoSe$_2$ on CC, designated as NiSe/CC and MoSe$_2$/CC, respectively (Fig. 1e).

Fig. 1f displays the TEM image of the nanowire with a diameter of about 100 nm and there are nanoparticles on the

nanowire similar to that revealed by SEM. To determine the composition and structure of the product, HR-TEM is performed as shown in Fig. 1g. The lattice spacing of 0.65 nm corresponds to the MoSe$_2$ (002) plane and that of 0.27 nm arises from the NiSe (101) plane furnishing evidence that NiSe particles are embedded in MoSe$_2$. Moreover, distortion is observed between the MoSe$_2$ (002) and NiSe (101) planes as shown by the dotted lines. The lattice mismatch of NiSe and MoSe$_2$ is calculated to be 11.25%. The distorted domain in the heterostructure enhances the catalytic activity and accelerates electron transfer compared to the pure phase catalysts.[27,28] The heterointerface of MoSe$_2$ (002) and NiSe (101) is adopted to construct the model (shown in Fig. S3†) according to the distorted domain. Fig. 1h depicts the optimized model of the heterointerface between the MoSe$_2$ (002) and NiSe (101) planes. Compared to the individual MoSe$_2$ (002) and NiSe (101) in Fig. 1i and j, there is an obvious rearrangement of the atoms near the interface as shown by the dotted/dashed rectangles. The results show the formation of a heterointerface between MoSe$_2$ and NiSe after selenation by in $situ$ phase separation similar to previous observations.[29,30] The elemental maps of Mo, Ni, and Se (Fig. S4†) confirm that the continuous and uniform MoSe$_2$ is composed of nanowires and the dispersed NiSe originates from the particles on the nanowires as shown by SEM (Fig. 1d) and TEM (Fig. 1f and g).

The Raman scattering spectra in Fig. 2a show the composition of NiSe and MoSe$_2$ in NMS. The peaks at 237 and 282 cm^{-1} are the A$_{1g}$ and E$^1_{2g}$ Raman modes of MoSe$_2$[31] and the peak near 266 cm^{-1} indicates the presence of NiSe.[32,33] The blueshifts observed from MoSe$_2$ in the heterostructure reveal the conversion from the 2H-phase into the 1T-phase leading to enhanced metallic behavior, which is expected to accelerate electrocatalysis.[34]
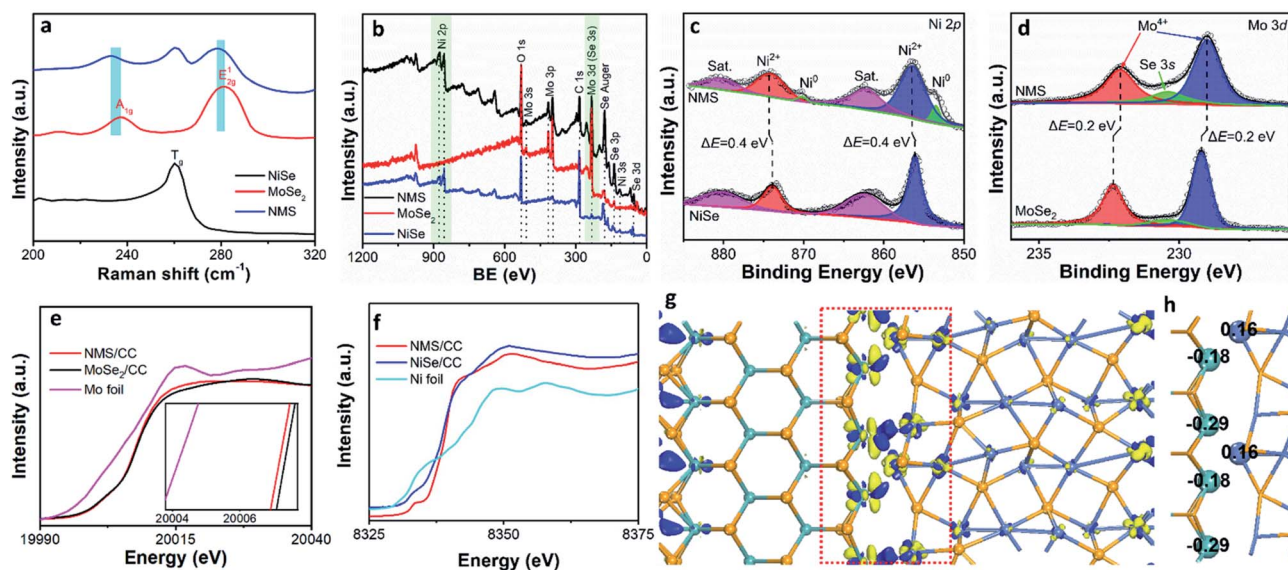

Fig. 2   (a) Raman scattering spectra of NMS/CC, MoSe$_2$/CC, and NiSe/CC; (b) XPS survey spectra; (c) Ni 2p spectra and (d) Mo 3d spectra of NMS/CC, MoSe$_2$/CC, and NiSe/CC; (e) Mo and (f) Ni K–edge XANES spectra of NMS/CC, MoSe$_2$/CC, and NiSe/CC; (g) electron density difference and (h) Mulliken charge analysis of the NiSe/MoSe$_2$ heterointerface (brown color represents Se, cyan represents Mo, bice represents Ni, and the blue and yellow regions represent electron accumulation and depletion, respectively).

The chemical composition of the samples is determined by X-ray photoelectron spectroscopy (XPS). The Ni 2p binding energies at 856.8/874.7 eV (Fig. S5a†) and Mo 3d binding energies at 232.4/235.6 eV (Fig. S5b†) are associated with Ni–O and Mo–O in NMO, respectively.[35–37] The survey spectrum of NMS/CC in Fig. 2b discloses the presence of Ni, Mo, and Se. The high-resolution Ni 2p spectrum of NMS/CC shifts by about 0.4 eV to higher binding energies than pure NiSe at 856.5/874.3 eV (Fig. 2c).[38] In contrast, the Mo 3d peaks of NMS/CC shift by about 0.2 eV to smaller energies compared to pure $MoSe_2$ (229.0/232.1 eV) (Fig. 2d).[39] Furthermore, the Ni and Mo K-edge X-ray absorption near edge structure (XANES) spectra show that the absorption edge of Mo in NMS/CC moves to a lower energy with respect to $MoSe_2$/CC (Fig. 2e), whereas Ni in NMS/CC shifts to a higher energy in comparison with NiSe/CC (Fig. 2f). The shifts suggest changes in the electron configurations of both Ni and Mo due to the interactions near the heterointerface in NMS/CC.

The simulated electron density difference in Fig. 2g verifies the strong atomic interactions near the $NiSe(101)/MoSe_2(002)$ interface, where the blue and yellow regions represent charge accumulation and depletion, respectively. Electrons are more likely to accumulate at the Mo sites of the $NiSe/MoSe_2$ hetero-interface. The Mulliken charge analysis in Fig. 2h corroborates electron transfer from Ni to Mo atoms at the $NiSe/MoSe_2$ heterointerface agreeing with the peak shifts in XPS and energy shift in XANES. Generally, the electronic structure impacts the electrocatalytic characteristics. For example, electron depletion at the Ni sites at the interface yields stronger oxidation activity, whereas electron accumulation at the Mo sites leads to enhanced electrocatalytic reduction thereby affecting the bifunctional catalytical properties of NMS/CC.[40,41]

3.2 MOR performance

The electrocatalytic properties of the NMS/CC electrocatalyst in the anodic oxidation reaction are evaluated in an electrolyte composed of KOH (1.0 M) and methanol (1.0 M). Fig. 3a shows that smaller potentials are required in the MOR than the OER for NMS/CC. The potential of the MOR is 15% smaller than that in the OER for a current density of 100 mA cm^{-2} and the Tafel slope of the OER is about 14 times larger than that of the MOR for NMS/CC as shown in Fig. 3b. The EIS results in Fig. 3c confirm the smaller charge transfer resistance in the MOR,
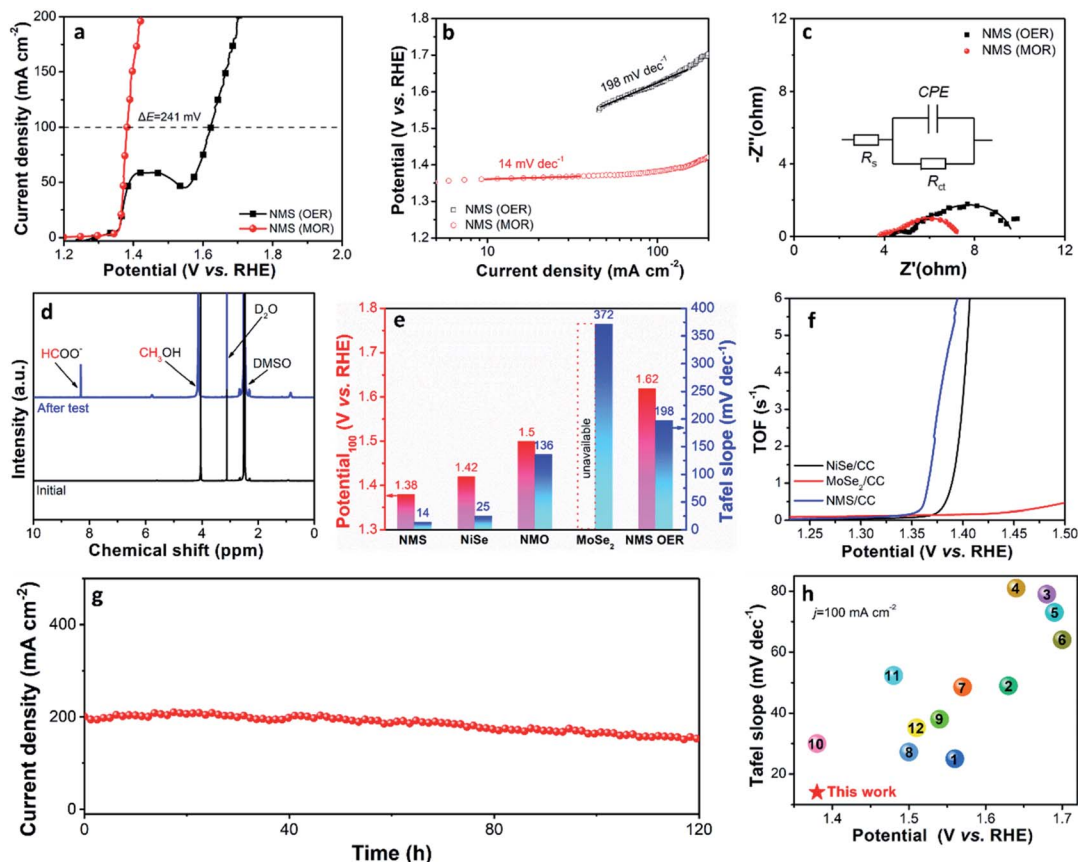

Fig. 3 (a) Polarization curves, (b) Tafel slope, and (c) EIS results of NMS/CC in the OER and MOR; (d) ^{1}H-NMR spectra of the electrolyte before and after the test; (e) comparison of the potentials (at a current density of 100 mA cm^{-2}) and Tafel slopes of the electrocatalysts; (f) potential-dependent turnover frequencies of NiSe/CC, MoSe$_2$/CC, and NMS/CC in the MOR; (g) stability of NMS/CC in the MOR; (h) comparison of the properties of NMS in this work with those of other reported electrocatalysts including (1) NiS/NF,[42] (2) Ni$_2$P-VP$_2$/NF,[43] (3) Co/CNFs(1000),[44] (4) Re/ReS$_2$-7H/CC,[45] (5) A-CNT-CoSnS,[46] (6) Ni MOF,[47] (7) NiFe LDH@NiCoP/NF,[48] (8) N–Fe$_2$PO$_{5−x}$-OT,[49] (9) DR-Ni$_3$FeN/N-G,[50] (10) pc-NiFe-LDH/NF,[51] (11) Ni$_3$FeN : Mo (5%),[52] and (12) S−CoFe-PBA/CFP.[53]

This journal is © The Royal Society of Chemistry 2022

J. Mater. Chem. A, 2022, **10**, 20761–20769 | **20765**

implying that replacing the OER with the MOR by introducing methanol into the electrolyte enhances the activity and kinetics of the anodic oxidation process. Compared to the violent bubble generation in the OER (Fig. S6a†), no bubbles can be found from the electrode in the MOR as shown in Fig. S6b.† ^{1}H-NMR conducted on the electrolyte after the MOR shows CHOO$^-$ (Fig. 3d), which is a value-added by-product used in industry and can be extracted and converted into formic acid. Therefore, replacing the OER with the MOR facilitates fast and energy-saving hydrogen production and at the same time, hydrogen is the only gaseous product obviating the need for further purification.

The polarization curves of NMS/CC, NiSe/CC, NMO/CC, and MoSe$_2$/CC for the MOR are presented in Fig. S7a.† NMS/CC requires 1.38 V *vs.* RHE to produce a current density of 100 mA cm^{-2} and it is distinctly smaller than those of NiSe/CC (1.42 V *vs.* RHE), MoSe$_2$/CC (unable to reach the current density), and NMO/CC (1.50 V *vs.* RHE). Fig. S7b† shows that the Tafel slope of NMS/CC is 14 mV dec^{-1} that is much smaller than those of NiSe/CC (25 mV dec^{-1}), NMO/CC (136 mV dec^{-1}), and MoSe$_2$/CC (372 mV dec^{-1}). Fig. 3e shows the potentials required for a current density of 100 mA cm^{-2} and the Tafel slopes of the electrocatalysts and corroborates the superior properties of NMS/CC in the MOR. Fig. S8a and b† disclose that NMS/CC has a smaller charge transfer resistance. Although the CC skeleton is electrochemically inert, its high electrical conductivity accelerates charge transfer, as indicated in Fig. S9.† The turnover frequency (TOF) is an important parameter to evaluate the intrinsic activity and a larger TOF translates into higher atom utilization efficiency and faster kinetics per active site. NMS/CC has higher intrinsic activity in the MOR (Fig. 3f) verifying that

the heterostructured NMS/CC electrocatalyst facilitates the dehydrogenation of methanol in comparison with individual NiSe/CC and MoSe$_2$/CC. It is because the distorted domain in the heterointerface and the change in the electronic structure of the metallic atoms enhance the intrinsic activity and accelerate charge transfer. The stability of the electrocatalyst is important for commercial adoption. Fig. 3g presents the chronoamperometric results of NMS/CC at 1.41 V *vs.* RHE in 1.0 M KOH and 1.0 M methanol. Highly stable MOR characteristics are observed from the current densities after operation for 120 h. The LSV curves of NMS/CC before and after the test are nearly the same (Fig. S10†), implying excellent stability of NMS/CC in the MOR. The anodic oxidation characteristics of NMS/CC and other non-noble transition metal-based electrocatalysts are compared in Fig. 3h and the former fares better than typical transition metal-based sulfides, phosphides, nitrides, oxides, and so on in anodic oxidation.

Potential-dependent Raman scattering spectra are acquired to study the reaction mechanism and intermediates in the MOR. Fig. 4a shows the OER results of NMS/CC in 1.0 M KOH. The two Raman peaks at 465 and 550 cm^{-1} increase at 1.40 V *vs.* RHE because of Ni–O vibration in Ni–OOH.[17] These two peaks become more intense gradually with applied potentials, suggesting that the oxidation of Ni and the formation of Ni–OOH are critical in the OER. Fig. 4b shows the MOR characteristics of NMS/CC in 1.0 M KOH and 1.0 M methanol. The Raman peaks at 2600–3000 cm^{-1} are the symmetrical and asymmetrical vibration modes of ν_s(CH) and ν_{as}(CH) for the surface C–H intermediates chemically adsorbing on the catalyst surface during the MOR. Methanol and intermediates adsorb on the metal (M) surface to form M-OCH$_x$ and undergo fast oxidation
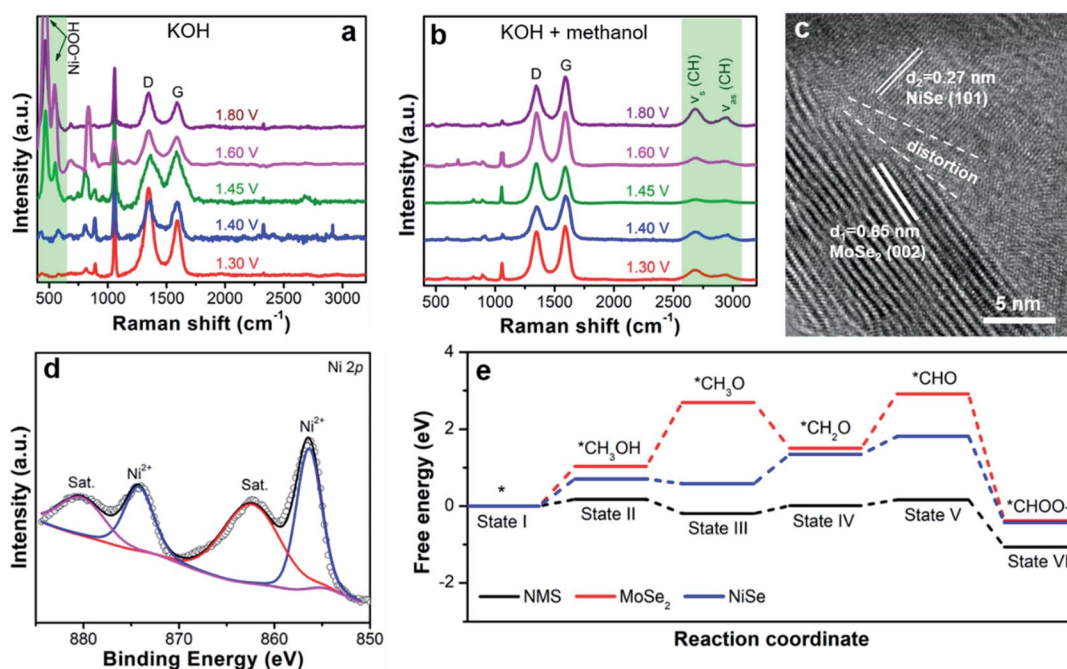

Fig. 4 (a) Potential-dependent Raman scattering spectra of the NMS/CC anode acquired using multiple potential steps in (a) 1.0 M KOH and (b) 1.0 M KOH/1.0 M methanol; (c) HR-TEM image and (d) XPS spectrum of the NMS/CC electrocatalyst after the stability test; (e) calculated MOR free energy profiles.

so that methanol is oxidized step by step. Therefore, the applied potentials are transferred completely to methanol and intermediates for their oxidation. Ni–OOH is not observed as the Raman spectra do not show peaks for Ni–OOH even at a high potential of 1.80 V *vs.* RHE. By adding methanol to the electrolyte, the energy applied can be used to oxidize methanol and C–H intermediates instead of metal atoms and consequently, charge transfer and mass conversion are improved. The structure and composition of NMS/CC after the stability test are determined and Fig. S11† indicates that the morphology of the nanowire arrays anchored with nanoparticles does not change. Fig. S12† shows that the electrocatalyst is composed of NiSe and MoSe$_2$ similar to the initial one, although weaker signals are detected because of surface oxidation[54] as indicated by the Mo 3d XPS and Raman spectra in Fig. S13.† The distortion of the NiSe(101)/MoSe$_2$(002) heterointerface can still be identified by HR-TEM as shown in Fig. 4c. The high-resolution XPS spectrum shows Ni^{2+} peaks at 856.4 and 874.3 eV (Fig. 4d) similar to the results obtained before the MOR. The results confirm that NMS/CC has outstanding long-term stability in the MOR because no gas is generated to avoid bubble overflow and the catalyst also undergoes no chemical change during the MOR.

To elucidate the catalytic mechanism of the NMS/CC heterostructured electrocatalyst in the MOR, density-functional theory (DFT) calculation is performed. The heterointerface comprising MoSe$_2$ (002) and NiSe (101) is applied to construct the model according to the distortion domain in HR-TEM (Fig. 1g). Fig. S14† shows the partial density of states of Ni-3d, Mo-4d, and Se-4p in the NMS heterostructure revealing strong hybridization between the metal-d and Se-p orbitals at the Fermi level. Fig. S15† shows the simulated schematic diagram of the corresponding catalyst in the MOR process. It is obvious that the Ni site is the active site for the MOR. However, MoSe$_2$ plays a significant role in tuning the electronic structure of Ni atoms at the interface, agreeing well with the Mulliken charge analysis, XPS, and XANES results. The free energy profiles of each step are illustrated in Fig. 4e. Compared to the individual NiSe and MoSe$_2$, the NMS heterostructure possesses the smallest adsorption free energy for methanol and enhanced methanol adsorption in the MOR. Furthermore, NMS shows a small positive reaction free energy of 0.21 eV for the first C–H bond breaking from state III to state IV. However, there are much higher positive reaction free energies of 0.76 eV for pure NiSe from state III to state IV (first C–H bond break) and 1.66 eV for pure MoSe$_2$ from state II to state III (O–H bond break). The calculation indicates that NMS with the heterointerface has better MOR activity due to stronger binding with reactants/intermediates stemming from the interactions of the atoms and electronic structure rearrangement near the heterointerface.

3.3 HER performance

The HER activity is explored. The polarization curves in Fig. S16a† show that the heterostructured NMS/CC electrocatalyst requires the smallest overpotential of 106 mV to generate a current density of 10 mA cm^{-2} in comparison with pure NiSe/CC (unavailable), MoSe$_2$/CC (237 mV), and NMO/CC (450 mV). The Tafel slope in Fig. S16b† further indicates faster hydrogen production kinetics on NMS/CC, which is as small as 104 mV dec^{-1}. Moreover, the larger TOF of NMS/CC gives rise to higher atom utilization efficiency and faster kinetics per active site in the HER (Fig. S17†), which is consistent with the smaller charge transfer resistance shown in Fig. S18.† The overpotentials of NMS/CC in a KOH/CH$_3$OH mixed electrolyte are slightly smaller than those in pure KOH (Fig. S19†) because the smaller surface tension of methanol than DW facilitates gas release from the catalyst surface. NMS/CC has a smaller overpotential and Tafel slope as illustrated in Fig. S20† in conjunction with superior stability for 24 h for the HER as shown in Fig. S21.† In addition, NMS/CC has a small $E_a + |E_c|$ for a separate MOR and HER as illustrated in Fig. S22,† suggesting that NiSe/CC has high MOR activity, whereas MoSe$_2$/CC performed excellently in the HER. Fig. S23 and S24† disclose that NMS/CC has a larger electrochemically active surface area. The results confirm that the heterostructured NMS/CC electrocatalyst has outstanding properties in both the MOR and the HER and demonstrate promising applications of the bifunctional electrocatalyst in the overall MOR/HER configuration.
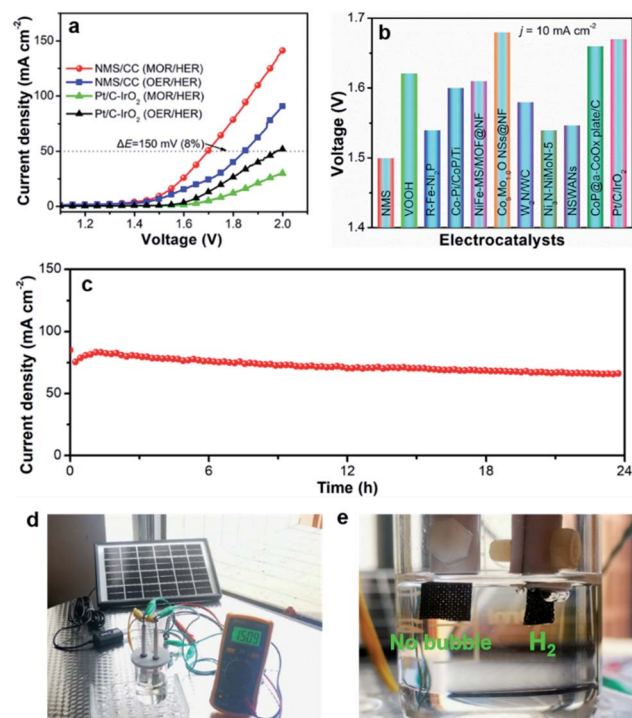

Fig. 5 (a) Polarization curves of the overall reaction; (b) comparison of the voltages required at a current density of 10 mA cm^{-2} in the overall reaction for the NMS/CC catalyst described in this work with those of previously reported catalysts such as VOOH,[55] R-Fe-Ni$_2$P,[56] Co-Pi/CoP/Ti,[57] NiFe-MS/MOF@NF,[58] Co$_5$Mo$_{1.0}$ONSs@NF,[59] W$_2$N/WC,[60] Ni$_3$N–NiMoN-5,[61] NSWANs,[62] and CoP@a-CoO$_x$ plate/C;[63] (c) long-term stability of the NMS/CC‖NMS/CC system for the overall reaction at a constant voltage of 1.8 V for 24 h; (d) photograph of the overall reaction system powered by a solar cell (1.5 V); (e) photograph showing the anode (left) and cathode (right) in (d).

3.4 Overall electrochemical performance

The overall reaction is monitored experimentally using NMS/CC as both the cathode and anode. The polarization curves in Fig. 5a show that the MOR/HER system needs lower voltages than the OER/HER, suggesting energy saving by the MOR/HER system. To generate a current density of 50 mA cm^{-2}, a voltage decrease of 8% can be achieved for the MOR/HER couple compared to the OER/HER couple. More importantly, the NMS/CC‖NMS/CC system is superior to commercial Pt/C‖IrO$_2$ and a smaller voltage is required for NMS/CC‖NMS/CC to produce a current density of 10 mA cm^{-2} in the overall reaction compared to other typical transition metal compounds in overall water splitting, as shown in Fig. 5b. The decline in the current response for the Pt/C‖IrO$_2$ catalysts in methanol may be attributed to the inhibition effect of the active sites because CH$_3$OH prefers to adsorb onto the IrO$_2$ surface and occupy active sites.[64] The chronopotentiometry curves in Fig. 5c also indicate that NMS/CC has outstanding long-term stability in the overall reaction because no obvious current density decay is found during the continuous 24 h measurement. To demonstrate the commercial viability, the NMS/CC‖NMS/CC overall reaction can be powered by a solar cell with an output voltage of 1.5 V (Fig. 5d) to produce hydrogen directly and bubbles are produced only on the cathode (Fig. 5e). All in all, the experimental and theoretical results confirm the large commercial potential of the MOR/HER couple for zero-carbon emission as well as other electrocatalytic and electro-synthetic applications.

4 Conclusions

A system integrating the MOR and HER and driven by solar cells shows energy-saving hydrogen production. The MOR and HER are co-catalyzed by a hierarchical heterostructure composed of NiSe and MoSe$_2$ prepared on CC. NiSe nanoparticles are anchored on MoSe$_2$ nanowires to facilitate fast charge transfer and improve physical stability. The electronic structure rearrangement and interactions between interfacial atoms are investigated experimentally and theoretically. The interactions of the atoms at the heterointerface balance the adsorption energy of the reactants/intermediates/products and promote the reaction kinetics in both HER and MOR. As a result, the NMS/CC electrocatalyst boasts higher efficiency in the MOR as revealed by a potential that is 15% less than that in the OER for a current density of 100 mA cm^{-2} together with a small Tafel slope (14 mV dec^{-1}) that is 7% of that in the OER. The MOR/HER couple which can be powered by a solar cell shows a decreased voltage of 8% compared to the OER/HER couple for hydrogen production and no further purification is needed. The results reveal the enormous application prospects of the MOR/HER couple for zero-carbon-emission energy systems and provide insights into the coordination of electrosynthesis and electrocatalysis.

Conflicts of interest

There are no conflicts to declare.

Notes and references

1 C. Chen, Y. Kang, Z. Huo, Z. Zhu, W. Huang, H. L. Xin, J. D. Snyder, D. Li, J. A. Herron and M. Mavrikakis, *Science*, 2014, **45**, 1339–1343.
2 X. Zou and Y. Zhang, *Chem. Soc. Rev.*, 2015, **44**, 5148–5180.
3 M. Yang, C. H. Zhang, N. W. Li, D. Luan, L. Yu and X. W. Lou, *Adv. Sci.*, 2022, **9**, 2105135.
4 J. A. Turner, *Science*, 2004, **305**, 972–974.
5 X. Peng, C. Pi, X. Zhang, S. Li, K. Huo and P. K. Chu, *Sustainable Energy Fuels*, 2019, **3**, 366–381.
6 W. Cheng, H. Zhang, D. Luan and X. W. Lou, *Sci. Adv.*, 2021, **7**, eabg2580.
7 X. Peng, X. Jin, B. Gao, Z. Liu and P. K. Chu, *J. Catal.*, 2021, **398**, 54–66.
8 S. Zhao, C. Tan, C.-T. He, P. An, F. Xie, S. Jiang, Y. Zhu, K.-H. Wu, B. Zhang and H. Li, *Nat. Energy*, 2020, **5**, 881–890.
9 B. Zhang, L. Wang, Z. Cao, S. M. Kozlov, F. P. García de Arquer, C. T. Dinh, J. Li, Z. Wang, X. Zheng and L. Zhang, *Nat. Catal.*, 2020, **3**, 985–992.
10 S. L. Zhang, X. F. Lu, Z. P. Wu, D. Luan and X. W. Lou, *Angew. Chem., Int. Ed.*, 2021, **60**, 19068–19073.
11 X. K. Wan, H. B. Wu, B. Y. Guan, D. Luan and X. W. Lou, *Adv. Mater.*, 2020, **32**, 1901349.
12 R. Hao, Q.-L. Feng, X.-J. Wang, Y.-C. Zhang and K.-S. Li, *Rare Met.*, 2022, **41**, 1314–1322.
13 H. Zhang, W. Zhou, X. F. Lu, T. Chen and X. W. Lou, *Adv. Energy Mater.*, 2020, **10**, 2000882.
14 Q. Xu, G. Qian, S. Yin, C. Yu, W. Chen, T. Yu, L. Luo, Y. Xia and P. Tsiakaras, *ACS Sustain. Chem. Eng.*, 2020, **8**, 7174–7181.
15 H. Jiang, M. Sun, S. Wu, B. Huang, C. S. Lee and W. Zhang, *Adv. Funct. Mater.*, 2021, **31**, 2104951.
16 X. Wei, Y. Li, L. Chen and J. Shi, *Angew. Chem., Int. Ed.*, 2021, **60**, 3148–3155.
17 B. Zhao, J. Liu, C. Xu, R. Feng, P. Sui, L. Wang, J. Zhang, J. L. Luo and X. Z. Fu, *Adv. Funct. Mater.*, 2021, **31**, 2008812.

20768 | *J. Mater. Chem. A*, 2022, **10**, 20761–20769

This journal is © The Royal Society of Chemistry 2022

18 X. Peng, Y. Yan, X. Jin, C. Huang, W. Jin, B. Gao and P. K. Chu, *Nano Energy*, 2020, **78**, 105234.

19 W.-L. Ding, Y.-H. Cao, H. Liu, A.-X. Wang, C.-J. Zhang and X.-R. Zheng, *Rare Met.*, 2021, **40**, 1373–1382.

20 X. Peng, Y. Yan, S. Xiong, Y. Miao, J. Wen, Z. Liu, B. Gao, L. Hu and P. K. Chu, *J. Mater. Sci. Technol.*, 2022, **118**, 136–143.

21 X. Peng, A. M. Qasim, W. Jin, L. Wang, L. Hu, Y. Miao, W. Li, Y. Li, Z. Liu, K. Huo, K. Y. Wong and P. K. Chu, *Nano Energy*, 2018, **53**, 66–73.

22 J. Jia, L. Zhao, Y. Chang, M. Jia and Z. Wen, *Ceram. Int.*, 2020, **46**, 10023–10028.

23 Q. Zhang, W. Xiao, W. H. Guo, Y. X. Yang, J. L. Lei, H. Q. Luo and N. B. Li, *Adv. Funct. Mater.*, 2021, **31**, 2102117.

24 L. Xia, H. Song, X. Li, X. Zhang, B. Gao, Y. Zheng, K. Huo and P. K. Chu, *Front. Chem.*, 2020, **8**, 382.

25 Y.-H. Kiang, W. Xu, P. W. Stephens, R. G. Ball and N. Yasuda, *Cryst. Growth Des.*, 2009, **9**, 1833–1843.

26 A. P. de Moura, L. H. de Oliveira, I. L. V. Rosa, C. S. Xavier, P. N. Lisboa-Filho, M. S. Li, F. A. La Porta, E. Longo and J. A. Varela, *Sci. World J.*, 2015, **2015**, 315084.

27 H. Yang, Y. Long, Y. Zhu, Z. Zhao, P. Ma, J. Jin and J. Ma, *Green Chem.*, 2017, **19**, 5809–5817.

28 X. Zheng, X. Han, Y. Cao, Y. Zhang, D. Nordlund, J. Wang, S. Chou, H. Liu, L. Li and C. Zhong, *Adv. Mater.*, 2020, **32**, 2000607.

29 X. Peng, L. Wang, L. Hu, Y. Li, B. Gao, H. Song, C. Huang, X. Zhang, J. Fu, K. Huo and P. K. Chu, *Nano Energy*, 2017, **34**, 1–7.

30 C. Huang, X. Miao, C. Pi, B. Gao, X. Zhang, P. Qin, K. Huo, X. Peng and P. K. Chu, *Nano Energy*, 2019, **60**, 520–526.

31 C.-T. Wu, S.-Y. Hu, K.-K. Tiong and Y.-C. Lee, *Results Phys.*, 2017, **7**, 4096–4100.

32 Y. Li, D. Yan, Y. Zou, C. Xie, Y. Wang, Y. Zhang and S. Wang, *J. Mater. Chem. A*, 2017, **5**, 25494–25500.

33 C. Liu, K. Wang, X. Zheng, X. Liu, Q. Liang and Z. Chen, *Carbon*, 2018, **139**, 1–9.

34 X. Zhang, Y. Y. Zhang, Y. Zhang, W. J. Jiang, Q. H. Zhang, Y. G. Yang, L. Gu, J. S. Hu and L. J. Wan, *Small Methods*, 2019, **3**, 1800317.

35 X. T. Wang, T. Ouyang, L. Wang, J. H. Zhong and Z. Q. Liu, *Angew. Chem., Int. Ed.*, 2020, **59**, 6492–6499.

36 X. Peng, X. Jin, N. Liu, P. Wang, Z. Liu, B. Gao, L. Hu and P. K. Chu, *Appl. Surf. Sci.*, 2021, **567**, 150779.

37 Z. Wang, J. Chen, E. Song, N. Wang, J. Dong, X. Zhang, P. M. Ajayan, W. Yao, C. Wang and J. Liu, *Nat. Commun.*, 2021, **12**, 1–10.

38 P. F. Liu, L. Zhang, L. R. Zheng and H. G. Yang, *Mater. Chem. Front.*, 2018, **2**, 1725–1731.

39 X. Wang, Y. Gong, G. Shi, W. L. Chow, K. Keyshar, G. Ye, R. Vajtai, J. Lou, Z. Liu, E. Ringe, B. K. Tay and P. M. Ajayan, *ACS Nano*, 2014, **8**, 5125–5131.

40 X. Zhou, Y. Liu, H. Ju, B. Pan, J. Zhu, T. Ding, C. Wang and Q. Yang, *Chem. Mater.*, 2016, **28**, 1838–1846.

41 Y. Jia, L. Zhang, G. Gao, H. Chen, B. Wang, J. Zhou, M. T. Soo, M. Hong, X. Yan and G. Qian, *Adv. Mater.*, 2017, **29**, 1700017.

42 Z. Pi and H. Zhong, *IOP Conf. Ser. Earth Environ. Sci.*, 2021, **651**, 042062.

43 H. Yan, Y. Xie, A. Wu, Z. Cai, L. Wang, C. Tian, X. Zhang and H. Fu, *Adv. Mater.*, 2019, **31**, 1901174.

44 Z. Yang, C. Zhao, Y. Qu, H. Zhou, F. Zhou, J. Wang, Y. Wu and Y. Li, *Adv. Mater.*, 2019, **31**, 1808043.

45 Q. Q. Pang, Z. L. Niu, S. S. Yi, S. Zhang, Z. Y. Liu and X. Z. Yue, *Small*, 2020, **16**, 2003007.

46 R. Jeyagopal, Y. Chen, M. Ramadoss, K. Marimuthu, B. Wang, W. Li and X. Zhang, *Nanoscale*, 2020, **12**, 3879–3887.

47 V. Maruthapandian, S. Kumaraguru, S. Mohan, V. Saraswathy and S. Muralidharan, *ChemElectroChem*, 2018, **5**, 2795–2807.

48 H. Zhang, X. Li, A. Hähnel, V. Naumann, C. Lin, S. Azimi, S. L. Schweizer, A. W. Maijenburg and R. B. Wehrspohn, *Adv. Funct. Mater.*, 2018, **28**, 1706847.

49 Y. Wu, Y. Meng, J. Hou, S. Cao, Z. Gao, Z. Wu and L. Sun, *Adv. Funct. Mater.*, 2018, **28**, 1801397.

50 S. Zhao, M. Li, M. Han, D. Xu, J. Yang, Y. Lin, N. E. Shi, Y. Lu, R. Yang and B. Liu, *Adv. Funct. Mater.*, 2018, **28**, 1706018.

51 H. Li, X. Wang, T. Wang and F. Xiao, *J. Alloys Compd.*, 2020, **844**, 156224.

52 X. Liu, X. Lv, P. Wang, Q. Zhang, B. Huang, Z. Wang, Y. Liu, Z. Zheng and Y. Dai, *Electrochim. Acta*, 2020, **333**, 135488.

53 J. Wang, M. Zhang, J. Li, F. Jiao, Y. Lin and Y. Gong, *Dalton Trans.*, 2020, **49**, 14290–14296.

54 M. Qiang, X. Zhang, H. Song, C. Pi, X. Wang, B. Gao, Y. Zheng, X. Peng, P. K. Chu and K. Huo, *Carbon*, 2022, **197**, 238–245.

55 H. Shi, H. Liang, F. Ming and Z. Wang, *Angew. Chem., Int. Ed.*, 2017, **56**, 573–577.

56 M. Li, J. Wang, X. Guo, J. Li, Y. Huang, S. Geng, Y. Yu, Y. Liu and W. Yang, *Appl. Surf. Sci.*, 2021, **536**, 147909.

57 L. Ai, Z. Niu and J. Jiang, *Electrochim. Acta*, 2017, **242**, 355–363.

58 M. Zhao, W. Li, J. Li, W. Hu and C. M. Li, *Adv. Sci.*, 2020, **7**, 2001965.

59 Y. Zhang, Q. Shao, S. Long and X. Huang, *Nano Energy*, 2018, **45**, 448–455.

60 J. Diao, Y. Qiu, S. Liu, W. Wang, K. Chen, H. Li, W. Yuan, Y. Qu and X. Guo, *Adv. Mater.*, 2020, **32**, 1905679.

61 A. Wu, Y. Xie, H. Ma, C. Tian, Y. Gu, H. Yan, X. Zhang, G. Yang and H. Fu, *Nano Energy*, 2018, **44**, 353–363.

62 H. Li, S. Chen, H. Lin, X. Xu, H. Yang, L. Song and X. Wang, *Small*, 2017, **13**, 1701487.

63 Q. Zhou, T.-T. Li, J. Qian, Y. Hu, F. Guo and Y.-Q. Zheng, *J. Mater. Chem. A*, 2018, **6**, 14431–14439.

64 Y.-Y. Hou, J.-M. Hu, L. Liu, J.-Q. Zhang and C.-N. Cao, *Electrochim. Acta*, 2006, **51**, 6258–6267.

This journal is © The Royal Society of Chemistry 2022

J. Mater. Chem. A, 2022, **10**, 20761–20769 | **20769**